
Article:
Meineke, J., Wenzel, F., de Marco, M. et al. (5 more authors) (2018) Motion artifacts in standard clinical setting obscure disease-specific differences in quantitative susceptibility mapping. Physics in Medicine & Biology, 63 (14). ISSN 0031-9155

https://doi.org/10.1088/1361-6560/aacc52

Motion Artifacts in Standard Clinical Setting Obscure Disease-Specific Differences in Quantitative Susceptibility Mapping

J. Meineke[1], F. Wenzel[1], M. De Marco[2], A. Venneri[2],

D.J. Blackburn[2], Kevin Teh[3], I.D. Wilkinson[3], U. Katscher[1]

[1]Hamburg, DE, Philips Research Europe, Tomographic Imaging, [2]Sheffield, GB, University of Sheffield, Department of Neuroscience, [3]Sheffield, GB, University of Sheffield, Academic Unit of Radiology

Abstract

Purpose: As Quantitative Susceptibility Mapping (QSM) is maturing, more clinical applications are being explored. With this comes the question whether QSM is sufficiently robust and reproducible to be directly used in a clinical setting where patients are possibly not cooperative and/or unable to suppress involuntary movements sufficiently.

Subjects and Methods: Twenty-nine patients with Alzheimer's Disease (AD), 31 patients with Mild Cognitive Impairment (MCI) and 41 healthy controls (HC) were scanned on a 3T scanner, including a multi-echo gradient-echo sequence for QSM and an inversion-prepared segmented gradient-echo sequence (T1-TFE, MPRAGE). The severity of motion artifacts (excessive/strong/noticeable/invisible) was categorized via visual inspection by two independent raters. Quantitative susceptibility was reconstructed using "Joint background-field removal and segmentation-Enhanced Dipole Inversion" (JEDI), based on segmented subcortical gray-matter regions, as well as using "Morphology Enabled Dipole Inversion" (MEDI). Statistical analysis of the susceptibility maps was performed per region.

Results: A large fraction of the data showed motion artifacts, visible in both magnitude images and susceptibility maps. No statistically significant susceptibility differences were found between groups including motion-affected data. Considering only subjects without visible motion, significant susceptibility differences were observed in caudate nucleus as well as in putamen.

Conclusion: Motion-effects can obscure statistically significant differences in QSM between patients and controls. Additional measures to restrict and/or compensate for subject motion should be taken for QSM in standard clinical settings to avoid risk of false findings.

1. Introduction

Numerous studies have reported elevated iron levels in deep gray matter nuclei of patients with Alzheimer's disease (AD), suggesting an important role of iron in the course of AD. Although it is not yet clarified if this role is a responsible or responsive one, an elevated iron level is known to be associated with elevated oxidative stress and neurotoxicity, and is thus implicated in particularly adverse progression of AD (for a review, see, e.g., Tao *et al* 2014).

The paramagnetic nature of iron leads to an increase of the tissue's magnetic susceptibility, and this increased susceptibility alters the phase pattern of gradient echo-based, T2*-weighted magnetic resonance (MR) images. The effect allows for the deduction of underlying susceptibility from quantitative assessment of variation in MR signal phase, providing an indirect estimate of tissue iron content. This quantitative deduction, called "Quantitative Susceptibility Mapping" (QSM), has been studied extensively in the past decade, and a number of specific QSM reconstruction algorithms have been developed (for reviews, see, e.g., Wang and Liu 2015, Deistung *et al* 2017). The current study is based on the QSM reconstruction algorithm "Joint background-field removal and segmentation-Enhanced Dipole Inversion" (JEDI, Meineke *et al* 2015, Meineke *et al* 2017), which makes use of *a priori* anatomical knowledge from automated brain structure segmentation as well as a single step formulation of the inverse field-to-source problem (Sharma *et al* 2015, Langkammer *et al* 2015, Liu *et al* 2014). For comparison, QSM reconstruction was performed using the "Morphology Enabled Dipole Inversion" (MEDI) algorithm (Liu *et al* 2012) as publicly available via the MEDI toolbox (Cornell MRI Research Lab, http://weill.cornell.edu/mri/pages/qsm.html).

QSM might be a suitable tool for mapping elevated iron levels in deep gray matter nuclei of AD patients, which would enable early and differential diagnosis of AD as well as monitoring disease progression. Since the introduction of QSM, several studies have been conducted to investigate brain iron in deep gray matter nuclei of AD patients (Acosta-Cabronero *et al* 2013, Moya *et al* 2014, van Bergen *et al* 2015, Moon *et al* 2016, Hwang *et al* 2017, Meineke *et al* 2017, Du *et al* 2017). However, drawing definite conclusions from these studies is hampered by several

drawbacks. First, all these studies included a limited number of patients / controls (between 16 and 53 subjects total). Second, four studies compared AD with controls (Acosta-Cabronero *et al* 2013, Moya *et al* 2014, Moon *et al* 2016, Meineke *et al* 2017), two studies compared patients with mild cognitive impairment (MCI) with controls (van Bergen *et al* 2015, Du *et al* 2017), and Hwang *et al* (2017) compared AD patients with patients who had dementia with Lewy bodies and Parkinson's disease. Some inconsistencies between iron levels in left and right hemisphere were observed by Du *et al* (2017), concluding that QSM can be *possibly* used in the diagnostic pathway for AD. All studies were *in vivo* studies except Moya *et al* (2014). The study with largest number of participants Meineke *et al* (2017) found no significant differences between groups. Nevertheless, significantly elevated iron was reported in five of these studies in the caudate nucleus (Acosta-Cabronero *et al* 2013, Moya *et al* 2014, van Bergen *et al* 2015, Moon *et al* 2016, Du *et al* 2017), in four studies in the putamen (Acosta-Cabronero *et al* 2013, Moya *et al* 2014, Moon *et al* 2016, Hwang *et al* 2017), in two studies in the amygdala (Acosta-Cabronero *et al* 2013, Hwang *et al* 2017), and in a single study in the dentate nucleus (Du *et al* 2017).

A possible and – to the best of our knowledge - yet unexplored reason for these diverse QSM results in AD patients is the impact of patient motion on QSM reconstruction. The current investigation was thus performed to inspect this potentially overlooked aspect, and analyzed the impact of patient motion on the accuracy of QSM reconstructions and the ability to discriminate between healthy and pathologic susceptibility distributions. MR measurements were acquired without pronounced precautions to reduce normal subject motion. The amount of motion was investigated *a posteriori*, and its impact on the mean reconstructed susceptibility per brain region was tested. In this study it was hypothesized that motion-effects would obscure statistically significant differences in QSM between the patient and control groups.

2. Materials and Methods

2.1 Subjects

Twenty-nine patients with mild to moderate AD (8 female, 21 male, age: mean 64±10 yrs, Mini-Mental-State-Examination (MMSE) = mean 19.2±3.2), 31 patients with MCI (15 female, 16 male,

age: mean 65±10 yrs, MMSE = mean 25.6±2.1), and 41 healthy controls (HC) (26 female, 15 male, age: mean 67±13 yrs, MMSE = mean 27.8±1.8) were scanned. Participants were told to not move during scanning, and cushions were placed on either side of the participant's head inside the RF head coil to limit subject motion. All participants were able to give written consent and informed consent was signed by all. The project received approval by the Yorkshire and Humber Regional Ethics Committee, Reference number: 12/YH/0474.

2.2 Data acquisition

Participants were scanned on a commercial 3T MR system (Ingenia, Philips Healthcare, Best, The Netherlands) using a 32-channel RF receive head-coil. Per subject, multiple scans were performed with an overall examination duration of roughly 60 minutes. From these scans, the following two scans were taken into account for this study:

- A multi-echo gradient-echo sequence (its phase serving as the basis for QSM reconstruction) with field of view (anterior-posterior, feet-head, left-right) = 240×145×210 mm, acquisition voxel 0.6×0.6×2.0 mm³ reconstructed to 0.6×0.6×1.0 mm³, flip angle = 14°, TE = 3.5 ms, ΔTE = 4 ms, 7 echoes, TR = 31 ms, bandwidth = 275 Hz/voxel, SENSE reduction factor (phase/slice) = 1.8×1.2, total scan time 6.5 minutes, true axial orientation. These parameters for the QSM scan allowed for optimal use of the available time by collecting as much data as possible using a bipolar readout sampling without flow-compensation. The choice of TR balanced the need for full-brain, high-resolution acquisition within a clinically acceptable time with the need for high sensitivity to subtle changes in the detectable MR signal phase. Prescribing the scan-orientation as axial with respect to the scanner magnetic field served the purpose of having the dipole patterns generated by the susceptibility distribution within the tissue aligned with the elongated voxels to avoid unnecessary errors from partial volume effects (Acosta-Cabronero *et al* 2013). This scan was performed at the end of the patient's examination.
- A T1-weighted, magnetization-prepared turbo field echo (TFE) sequence (serving as the basis for model-based segmentation of brain structures) with field of view (anterior-posterior, feet-head, left-right) = 240×240×170 mm, acquisition voxel 0.94×0.94×1.0 mm³,

flip angle = 8°, TE = 3.7 ms, TR = 8.0 ms, TFE factor=222, inversion delay = 1000 ms, bandwidth = 191.5 Hz/voxel, SENSE reduction factor (phase/slice) = 1.0×2.2. This scan was performed at the beginning of the patient's examination.

To compensate for potential head motion between scans, a rigid registration of the T1-weighted scan and the magnitude of the first echo of the QSM sequence was performed using in-house registration software. It optimized the six degrees of freedom of a rigid transformation by gradient descent with respect to normalized mutual information, a measure describing the entropy of the joint intensity histogram (Viola and Wells 1997). The software was successfully applied to other registration tasks recently (Wenzel *et al* 2010, Netsch *et al* 2000).

2.3 Anatomical Segmentation

Fully automated anatomical segmentation was performed on the T1-weighted TFE scans using a shape-constrained deformable surface model (Wenzel *et al* 2018). For region-based statistical analysis, labels of sufficiently large deep gray matter structures (globus pallidus, caudate nucleus, putamen, hippocampus, and thalamus) were mapped onto QSM orientation via the estimated transformation from the rigid registration step. The segmentation also generates a binary mask labeling the brain, which was used to define the region of interest (ROI), in which susceptibility values were reconstructed. An example segmentation is shown in Fig. 1. The accuracy of the segmentation was assessed visually for all cases.

2.4 QSM reconstruction

This study employed a single-step algorithm, based on the JEDI algorithm (Meineke *et al* 2015, Meineke *et al* 2017), for QSM reconstruction. Briefly, the tissue susceptibility χ was estimated solving the regularized minimization problem

$$\chi = \arg\min_{\chi}\left\{\left\|W\left(\frac{B_0\gamma}{2\pi}L\otimes D\otimes\chi - L\otimes f_{\text{tot}}\right)\right\|_2^2 + \lambda\left\|M_E\mathbf{G}\chi\right\|_2^2\right\}$$

using a preconditioned conjugate-gradient method (Bilgic *et al* 2014) with reweighting similar to Liu *et al* (2013). In the data-term, f_{tot} is the measured (wrapped) off-resonance field, L the Laplace

operator, D the dipole-operator expressed as $\hat{D} = 1/3 - k_z^2 / \mathbf{k}^2$ in Fourier-space (Marques and Bowtell 2005), and W is a weighting matrix reflecting the uncertainty deriving from the measured field map. It was computed using Gaussian error propagation by convolving the variance of f_{tot} with L^2. B_0 is the main magnetic field strength of the scanner, and γ the gyromagnetic ratio. In the regularization term, λ=0.01 is the regularization parameter, $\mathbf{G}$ the gradient operator in three dimensions and M_E is an edge-weighting matrix, described in more detail below. λ was chosen to maximize the accuracy of the reconstruction in a numerical phantom, and by visual inspection of reconstructed *in vivo* susceptibility maps. The Laplace operator L was implemented as a noise-robust, computationally efficient second-order derivative kernel of minimal footprint (3x3x3 voxels) to reduce effects of measurement noise (van Lier *et al* 2012). This minimal footprint has the advantage of increased robustness to noise in the measured field-map by averaging in the directions orthogonal to the differentiation, while avoiding the possible issue of mapping high-frequency noise components of the susceptibility distribution to zero. For the application of L, the need for separate global spatial unwrapping was circumvented by locally shifting all values of f_{tot} within the footprint of L by the value of the central voxel (modulo the bandwidth given by 2π/ΔTE). As a result, the central voxel equals zero and the remaining field variation within the footprint of L is within $\pm\pi$ for typical field gradients in the brain and sequence parameters employed here. In this way, a separate spatial unwrapping and possibly resulting systematic errors (Robinson *et al* 2017) were avoided.

The edge-weighting mask M_E contained additional information about the geometry of the susceptibility distribution containing values between zero (allowing edges in the susceptibility) and one (penalizing edges in the susceptibility). This was crucial to avoid a systematic underestimation of susceptibility differences across tissue boundaries. To compute M_E, edge-information was derived from the magnitude of the last echo (T_E=27 ms) as well as from a preliminary susceptibility distribution (reconstructed without any edge-information, i.e. setting M_E=1) as follows: After computing the magnitude of the gradient using Sobel filters, the obtained values were mapped to the unit interval by thresholding and linear interpolation between minimum and maximum values given by the 50th and 95th percentile of the gradient magnitude map. The resulting edge-weighting

images for each prior were finally combined using pointwise multiplication. In addition, edge-information from the above-described segmentation was incorporated by setting M_E at location of edges in the region-labels to 0.1.

For comparison, QSM reconstruction was performed using MEDI (Liu *et al* 2012) in combination with the Laplacian Boundary Value (LBV) method (Zhou *et al* 2014) as implemented in the employed MEDI toolbox, keeping the default regularization parameter equal to 1000.

Subsequent to QSM reconstructions, the mean susceptibility was computed within the segmented regions, referencing to the mean of the susceptibility in the corpus callosum. The corpus callosum was chosen as reference as suggested by Bilgic *et al* (2012) due to its higher stability compared to other reference tissues applied, such as cerebrospinal fluid.

2.5 Statistical Analysis

The null-hypothesis, i.e. that the samples of the mean susceptibility values for different patient groups can be considered as drawn from the same distribution, was tested using Welch's t-test for each region separately. A p-value smaller than 0.05 was considered to indicate a statistically significant difference. To account for multiple comparisons, the Bonferroni correction was applied. The distribution of mean susceptibilities within each group was used to compute the Area Under the receiver operating characteristic Curve (AUC). Based on the underlying nonparametric Mann-Whitney U statistics, the AUC can be interpreted as the probability that a randomly chosen diseased subject is rated as more likely to be diseased than a randomly chosen non-diseased subject (Hanley and McNeil 1982).

2.6 Motion rating

The severity of motion artifacts was categorized using magnitude images of the QSM scans at TE=27 ms by two independent, experienced observers using four motion categories: invisible / noticeable / strong / excessive motion. A region-based statistical analysis of the susceptibility maps was performed for subjects which both observers rated as invisible motion (called invisible-motion group, IMG), as well as for all subjects excluding only those subjects which at least one of the observers rated as excessive motion (called acceptable-motion group, AMG). These subjects,

which at least one of the observers rated as excessive motion, were excluded from further analysis. In spite of being a subjective method, visual inspection by experienced readers is still the gold standard for artifact rating due to the lack of a consistently reliable numerical method to extract and quantify motion errors from MR images in a fully automated fashion. Example images of the first three motion categories are given in Fig. 2. Please note that motion artifacts present in magnitude images and susceptibility maps do not need to be directly related since, for example, the QSM reconstruction algorithm might reject phase patterns that do not match the dipole kernel.

3. Results

Due to excessive motion, five subjects from the AD group, five subjects from the MCI group, and four subjects from the HC group were excluded from further analysis. From the remaining AMG (87 subjects in total), only 24 subjects showed no obvious motion effects, forming the IMG. The percentage of subjects with invisible motion (as well as the percentage of subjects with excessive motion) is roughly the same for AD, MCI, and HC. Table 1 summarizes statistics about the motion and subject groups. Subject groups were age-matched via subject selection designed for this study. Motion groups were created without explicit selection by subjects' age, but are still sufficiently age-matched. According to Acosta-Cabronero *et al* (2016), Hallgren and Sourander (1958), the remaining differences in age lead to an uncertainty in susceptibility, which is far too low to be relevant for the results of the current study.

Figure 3 shows box-and-whisker plots of the mean susceptibility in segmented deep gray matter structures. Including Bonferroni correction, a statistically significant difference (i.e., $p<0.05$) was observed only in the mean susceptibility of the caudate nucleus between the AD and HC groups for IMG using JEDI. Without Bonferroni correction, $p<0.05$ was observed not only for this case (yielding $p=0.002$, Area Under Curve of Receiver Operating Characteristic AUC=0.94), but also for the putamen ($p=0.013$, AUC=0.94) between the AD and HC groups for IMG using JEDI, and in caudate nucleus ($p=0.016$, AUC=0.86) between AD and MCI groups for IMG using JEDI. No brain region with statistically significant susceptibility difference was found between MCI and HC for IMG (neither for JEDI nor LBV-MEDI). For AMG, no statistically significant differences were found for

any segmented brain regions between all subject groups (again neither for JEDI nor LBV-MEDI, i.e., all AUC between 0.4 and 0.6). In general, a trend of AMG towards larger susceptibility span is observed for boxes, whiskers, and outliers, in comparison to IMG.

An overview of all p-values obtained is given in Tab. 2.

4. Discussion and Conclusion

This study investigated the role of patient motion for QSM reconstruction stability with respect to differentiation between different pathological groups in the context of AD. The susceptibility differences expected between patients and controls were only found when all subjects showing any motion were excluded. This suggests that motion has a highly influential and in this case adverse effect on susceptibility reconstruction and quantitation.

To investigate the possibility that the choice of QSM reconstruction influenced the obtained results, QSM was performed using two different reconstruction methods: the recently introduced JEDI (Meineke *et al* 2015, Meineke *et al* 2017) and the widely adopted MEDI (Liu *et al* 2012) algorithm combined with LBV for background-field removal (Zhou *et al* 2014). Both reconstruction methods find differences with non-Bonferroni corrected p-values < 0.05 in the caudate nucleus and the putamen only between AD and HC groups for the IMG. Including the Bonferroni-correction, the JEDI method finds $p < 0.05$ in the caudate nucleus between AD and HC groups. The fact that neither method is able to observe a significant difference between the patient groups in the AMG suggests that this finding is indeed due to motion effects in the original data, rather than the specific QSM reconstruction algorithm.

It has been suggested in the literature that the use of L2-regularization leads to systematic underestimation of susceptibility differences across tissue-boundaries (Deverdun *et al* 2017, Bilgic *et al* 2012, Liu *et al* 2012). However, this finding can be attributed to a large extent to the absence of prior information in the L2-regularization term. In the JEDI method, this effect is mitigated by the use of high-quality edge-weighting in the L2-regularization term. The JEDI results do not show severe underestimation of the susceptibility, but have the benefit of a more natural appearance compared to the L1-regularization, which promotes piece-wise constant solutions (Acosta-

Cabronero *et al* 2013). Furthermore, as stated above, our technique for avoiding phase unwrapping is limited by the assumption that the occurring field gradient is sufficiently small. The field differences between adjacent voxels must be smaller than half the bandwidth of the field map. For the voxel size and ΔTE employed in this study, this results in maximally allowed field gradients of roughly 60 Hz/mm, whereas typical maximum field gradients in the brain (around nasal cavities) have not been observed to exceed 20 Hz/mm. It can thus be expected that the field requirements described are fulfilled.

In the framework of this study, which was carried out without pronounced precautions for motion suppression or motion compensation, only 24% of 101 subjects scanned showed invisible motion. Thus, even starting with a high number of subjects (higher than in all comparable studies before, Acosta-Cabronero *et al* 2013, Moya *et al* 2014, van Bergen *et al* 2015, Moon *et al* 2016, Hwang *et al* 2017, Meineke *et al* 2017, Du *et al* 2017), the resulting subject groups with invisible motion are relatively small, which limits the reliability of conclusions. Furthermore, it cannot be excluded that the observed changes in putamen / caudate susceptibility are not caused by the motion state but by other, physiologic reasons, or purely random. However, it can be taken as a trend that putamen and caudate nuclei are the brain regions most frequently reported as demonstrating susceptibility differences in former studies (Acosta-Cabronero *et al* 2013, Moya *et al* 2014, van Bergen *et al* 2015, Moon *et al* 2016, Hwang *et al* 2017, Meineke *et al* 2017, Du *et al* 2017). Of particular note, the *post mortem* study in Moya *et al* (2014) (automatically excluding physiological motion-induced artefacts) reported a statistically significant susceptibility difference for these two regions. This additionally motivates the hypothesis of this study that motion detrimentally influences calculated susceptibility variance, increasing the likelihood of motion being responsible for ‘hiding’ expected susceptibility differences.

The results of this study are not fully in line with a number of previously published results. However, the comparison of all previous studies does not yield a consistent result as discussed above, and the current study offers a potential explanation for this unsatisfying situation. Studies of course always differ in technical design, and these differences increase the risk of producing inconsistent results (Langkammer *et al* 2018). The current study tried to reduce this risk as far as

possible by including two – conceptually different – QSM reconstruction algorithms, yielding similar conclusions.

Thus, it seems to be highly recommended for QSM to apply additional measures to restrict patient motion during scanning, or to apply retrospective correction of the raw data as suggested by, for example, Feng *et al* (2017). Another, simple approach for reducing motion during the QSM scan would be to shift the scan towards the beginning of the examination. In the current study, the QSM scan was performed at the end of an examination lasting 60 minutes in total, which might increase motion probability of patients possibly not cooperative and/or unable to suppress involuntary movements sufficiently. In fact no obvious motion artifacts were observed for the T1-weighted scan used for segmentation, which was acquired at the very beginning of the examination.

This study focused on the investigation of susceptibility associated with deep gray matter nuclei, triggered by numerous studies discussing altered iron concentration for AD patients in these regions. The effects of altered iron concentration have also been investigated in cortical gray matter (Deistung *et al* 2015). A potentially higher impact of AD-related variance in cortical iron concentration could make investigation of the cortex a better target for AD diagnosis. However, cortical areas are particularly susceptible to QSM reconstruction imperfections, counter-balancing the potential advantage of any pronounced iron increase within these areas.

In conclusion, motion-effects seem to be able to obscure statistically significant differences in QSM between patients and controls. To avoid risk of false-negative findings, it seems to be highly recommended to apply suitable measures to reduce and/or compensate motion effects when acquiring or analyzing QSM images.

Acknowledgements

This study was funded by the European Union's Seventh Framework Programme (FP7/2007 – 2013) as part of the project VPH-DARE@IT (grant agreement no. 601055). The authors cordially thank Steven Wood for supporting organization of patient data, the radiographic skills of the

University of Sheffield MRI Unit, and Martin Bergtholdt and Thomas Stehle for supporting application of brain segmentation. IDW acknowledges support of the Wellcome Trust. AV, DJB and IDW also acknowledge the support of the NIHR Sheffield Biomedical Research Centre (Neuroscience) and of the NIHR Clinical Research Facility – Sheffield Teaching Hospital. The authors cordially thank the Cornell MRI Research Lab for providing access to the MEDI toolbox.

References

Acosta-Cabronero J, Williams GB, Cardenas-Blanco A, Arnold RJ, Lupson V, Nestor PJ. In Vivo Quantitative Susceptibility Mapping (QSM) in Alzheimer's Disease. PloS. ONE. 2013; 8: e81093. [PubMed: 24278382]

Acosta-Cabronero J, Betts MJ, Cardenas-Blanco A, Yang S, Nestor PJ. In Vivo MRI Mapping of Brain Iron Deposition across the Adult Lifespan. J. Neurosci. 2016; 36: 364-74. [PubMed: 26758829]

Bilgic B, Pfefferbaum A, Rohlfing T, Sullivan EV, Adalsteinsson E. MRI estimates of brain iron concentration in normal aging using quantitative susceptibility mapping. Neuroimage. 2012; 59: 2625-35. [PubMed: 24259479]

Bilgic B, Fan AP, Polimeni JR, Cauley SF, Bianciardi M, Adalsteinsson E, Wald LL, Setsompop K. Fast quantitative susceptibility mapping with L1-regularization and automatic parameter selection. Magn. Reson. Med. 2014; 72: 1444-59. [PubMed: 24259479]

Deistung A, Schäfer A, Schweser F, Reichenbach JR. Cortical Mapping of Magnetic Susceptibility and R2* Reveals Insights Into Tissue Composition. Proc. 23rd Annu. Meeting ISMRM.; Toronto, Canada. 20 May – 5 June.2015. p. 284.

Deistung A, Schweser F, Reichenbach JR. Overview of quantitative susceptibility mapping. NMR Biomed. 2017; 30: e3569. [PubMed: 27434134]

Deverdun J, Molino F, Menjot de Champfleur N, Le Bars E. Validation of a quantitative susceptibility mapping acquisition and reconstruction pipeline using a new iron sucrose based MR susceptibility phantom. J Neuroradiol. 2017; 44: 269-72.

[PubMed: 28215716]

Du L, Zhu Y, Song T, Xie L, Ma G. Subcortical Nuclei Iron Deposition of Alzheimer's Patients On MRI-QSM: Maybe a Diagnostic Indicator. Proc. 25th Annu. Meeting ISMRM.; Honolulu, HI. 22-27 April.2017. p. 2368.

Feng X, Loktyushin A, Deistung A, Reichenbach J. Image Quality Improvement by Applying Retrospective Motion Correction on Quantitative Susceptibility Mapping and R2*. Proc. 25th Annu. Meeting ISMRM.; Honolulu, HI. 22-27 April.2017. p. 3654.

Hallgren B, Sourander P. The effect of age on the non-haemin iron in the human brain. J. Neurochem. 1958; 3: 41-51. [PubMed: 13611557]

Hanley JA, McNeil BJ The meaning and use of the area under a receiver operating characteristic (ROC) curve. Radiology. 1982; 143: 29-36. [PubMed: 7063747]

Hwang EJ, Choi HS, Jang JH, Jung SE, Jung SL, Ahn KJ, Kim BS, Kim JS. Differentiation of Deep Gray Matters in Patients with Alzheimer's Disease (AD), Dementia with Lewy Bodies (DLB) and Parkinson's Disease Dementia (PDD) Using T1 Weighted Images and Quantitative Susceptibility Maps (QSM). Proc. 25th Annu. Meeting ISMRM.; Honolulu, HI. 22-27 April.2017. p. 4139.

Langkammer C, Bredies K, Poser BA, Barth M, Reishofer G, Fan AP, Bilgic B, Fazekas F, Mainero C, Ropele S. Fast quantitative susceptibility mapping using 3d EPI and total generalized variation. NeuroImage. 2015; 111: 622-30. [PubMed: 25731991]

Langkammer C, Schweser F, Shmueli K, Kames C, Li X, Guo L, Milovic C, Kim J, Wei H, Bredies K, Buch S, Guo Y, Liu Z, Meineke J, Rauscher A, Marques JP, Bilgic B. Quantitative susceptibility mapping: Report from the 2016 reconstruction challenge. Magn Reson Med. 2018; 79: 1661-73. [PubMed: 28762243]

Liu J, Liu T, de Rochefort L, Ledoux J, Khalidov I, Chen W, Tsiouris AJ, Wisnieff C, Spincemaille P, Prince MR, Wang Y. Morphology enabled dipole inversion for quantitative susceptibility mapping using structural consistency between the magnitude image and the susceptibility map. Neuroimage. 2012; 59: 2560-68. [PubMed: 21925276]

Liu T, Wisnieff C, Lou M, Chen W, Spincemaille P, Wang Y. Nonlinear formulation of the magnetic field to source relationship for robust quantitative susceptibility mapping: Magn. Reson. Med. 2013; 69: 467-76. [PubMed: 22488774]

Liu T, Zhou D, Spincemaille P, Wang Y. Differential approach to quantitative susceptibility mapping without background field removal. Proc. 22nd Annu. Meeting ISMRM.; Milan, Italy. 10-16 May.2014. p. 597.

Marques JP, Bowtell RW. Application of a Fourier-based method for rapid calculation of field inhomogeneity due to spatial variation of magnetic susceptibility. Conc. Magn. Reson. Part B: Magn. Reson. Engin. 2005; 25B: 65-78.

Meineke J, Senegas J, Katscher U, Wenzel F. Quantitative Susceptibility Mapping using Segmentation-Enabled Dipole Inversion. Proc. 23rd Annu. Meeting ISMRM.; Toronto, Canada. 20 May – 5 June.2015. p. 3321.

Meineke J, Wenzel F, Wilkinson ID, Katscher U. No Significant Increase of Magnetic Susceptibility Found in Subcortical Gray Matter of Patients with Alzheimer's Disease. Proc. 25th Annu. Meeting ISMRM.; Honolulu, HI. 22-27 April.2017. p. 2348.

Moon Y, Han SH, Moon WJ. Patterns of Brain Iron Accumulation in Vascular Dementia and Alzheimer's Dementia Using Quantitative Susceptibility Mapping Imaging. J. Alzheimers Dis. 2016; 51:737-45. [PubMed: 26890777]

Moya EA, Bennett DA, Schneider JA, Kotrotsou A, Dawe RJ, Arfanakis K. Magnetic Susceptibility in Subcortical Gray Matter Is Associated with Alzheimer's Pathology: An Ex-Vivo QSM-Pathology Investigation in a Community Cohort. Proc. 22nd Annu. Meeting ISMRM.; Milan, Italy. 10-16 May.2014. p. 1946.

Netsch T, Roesch P, Weese J, van Muiswinkel A, Desmedt P. Grey-value-based 3D registration of functional MRI time-series: comparison of interpolation order and similarity measure. Proc. SPIE 3979.; San Diego, CA. 6 June.2000. pp. 1148-59.

Robinson SD, Bredies K, Khabipova D, Dymerska B, Marques JP, Schweser F. An illustrated comparison of processing methods for MR phase imaging and QSM: combining array coil signals and phase unwrapping. NMR Biomed. 2017; 30. doi:

10.1002/nbm.3601. [PubMed: 27619999]

Sharma SD, Hernando D, Horng DE, Reeder SB. Quantitative susceptibility mapping in the abdomen as an imaging biomarker of hepatic iron overload. Magn. Reson. Med. 2015; 74: 673-83. [PubMed: 25199788]

Tao Y Wang Y, Rogers JT, Wang F. Perturbed iron distribution in Alzheimer's disease serum, cerebrospinal fluid, and selected brain regions: a systematic review and meta-analysis. J. Alzheimers Dis. 2014; 42: 679–90. [PubMed: 24916541]

van Bergen JM, Li X, Wyss M, Schreiner SJ, Steininger SC, Gietl AF, Treyer V, Leh SE, Buck F, Hua J, Nitsch R, Prüssmann KP, van Zijl P, Hock C, Unschuld PG. Regional Cerebral Iron Concentrations as Indicated by Magnetic Susceptibilities Measured with Quantitative Susceptibility Mapping (QSM) at 7 Tesla Correlate with Brain Aβ Plaque Density as Measured by 11-C-Pittsburgh Compound B Positron-Emission-Tomography (PiB-PET) in Elderly Subjects at Risk for Alzheimer's Disease (AD). Proc. 23rd Annu. Meeting ISMRM.; Toronto, Canada. 20 May – 5 June.2015. p. 400.

van Lier AL, Brunner DO, Pruessmann KP, Klomp DW, Luijten PR, Lagendijk JJ, van den Berg CA. B1+ phase mapping at 7 T and its application for in vivo electrical conductivity mapping. Magn. Reson. Med. 2012; 67: 552-61. [PubMed: 21710613]

Viola P, Wells WM. Alignment by Maximization of Mutual Information. Int. J. Comp. Vis. 1997; 24: 137–54.

Wang Y, Liu T. Quantitative susceptibility mapping (QSM): Decoding MRI data for a tissue magnetic biomarker. Magn. Reson. Med. 2015; 73: 82-101. [PubMed: 25044035]

Wenzel F, Young S, Wilke F, Apostolova I, Arlt S, Jahn H, Thiele F, Buchert R. B-spline-based stereotactical normalization of brain FDG PET scans in suspected neurodegenerative disease: impact on voxel-based statistical single-subject analysis. Neuroimage. 2010; 50: 994-1003. [PubMed: 20053378]

Wenzel F, Meyer C, Stehle T, Peter J, Siemonsen S, Thaler C, Zagorchev L. Rapid fully automatic segmentation of subcortical brain structures by shape-constrained surface adaptation. Medical Image Analysis. 2018; 46: 146-61. [PubMed: 29550581]

Zhou D, Liu T, Spincemaille P, Wang Y. Background field removal by solving the Laplacian boundary value problem. NMR Biomed. 2014; 27: 312-9. [PubMed: 24395595]

Figures and tables

motion groups	AD	MCI	HC
invisible motion	N=6 (58±6yrs)	N=8 (63±6yrs)	N=10 (59±7yrs)
acceptable motion	N=24 (65±10yrs)	N=26 (65±10yrs)	N=37 (68±12yrs)
excessive motion	N=5 (63±5yrs)	N=5 (62±8yrs)	N=4 (57±11yrs)

AD, Alzheimer‘s disease; MCI, Mild cognitive impairment; HC, Healthy controls

Tab. 1: Statistical overview of groups. For each AD, MCI, and HC group, number of subjects is given as well as average and standard deviation of age.

	motion groups	patient groups	caudate nucleus	globus pallidus	hippo-campus	putamen	thalamus
JEDI	invisible motion	AD vs HC	0.0018**	0.3080	0.7292	0.0126*	0.3236
		AD vs MCI	0.0163*	0.1220	0.3505	0.1217	0.2972
		MCI vs HC	0.5033	0.1449	0.5429	0.1842	0.7635
	acceptable motion	AD vs HC	0.7014	0.2502	0.7303	0.3313	0.0528
		AD vs MCI	0.4927	0.8426	0.2795	0.8424	0.1054
		MCI vs HC	0.2682	0.2979	0.3222	0.2463	0.8656
MEDI	invisible motion	AD vs HC	0.0392*	0.8163	0.8879	0.0232*	0.3689
		AD vs MCI	0.2927	0.2587	0.6308	0.2005	0.9701
		MCI vs HC	0.6026	0.1110	0.7037	0.2065	0.4509
	acceptable motion	AD vs HC	0.5175	0.3167	0.7544	0.5951	0.2939
		AD vs MCI	0.2916	0.7013	0.8783	0.3999	0.8387
		MCI vs HC	0.0981	0.6284	0.6831	0.2114	0.2744

AD, Alzheimer‘s disease; MCI, Mild cognitive impairment; HC, Healthy controls; JEDI, Joint background-field removal and segmentation-Enhanced Dipole Inversion; MEDI, Morphology Enabled Dipole Inversion

Tab. 2: Overview of p-values comparing different patient groups for all brain regions investigated and for both reconstruction algorithms applied, separately for the two motion groups. Double (single) stars indicate statistically significant susceptibility differences with (without) Bonferroni correction.

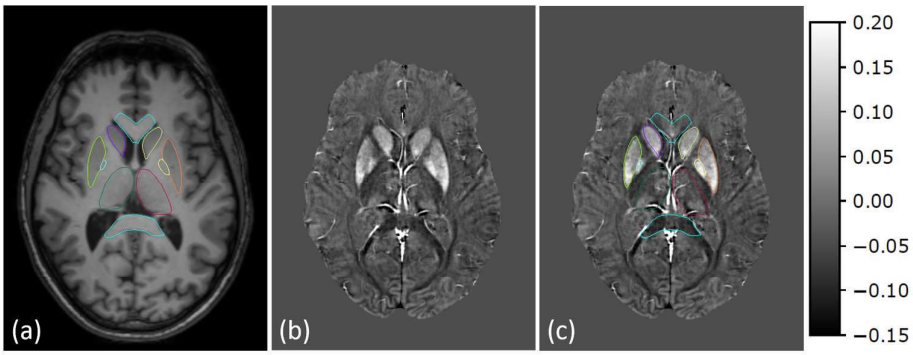

Fig. 1: Example result of anatomical segmentation and QSM reconstruction with JEDI. T1-weighted brain scan with segmented sub-cortical areas (a); reconstructed susceptibility map (b); susceptibility map with segmented sub-cortical areas (c). The grayscale mapping to susceptibility values in ppm is shown on the right-hand side. Regions shown are corpus callosum (cyan), putamen (light green and orange), caudate nucleus (purple and yellow), globus pallidus (light blue and light yellow) and thalamus (dark green and red). Not visible in the shown images, but used for statistical analysis, is the hippocampus.

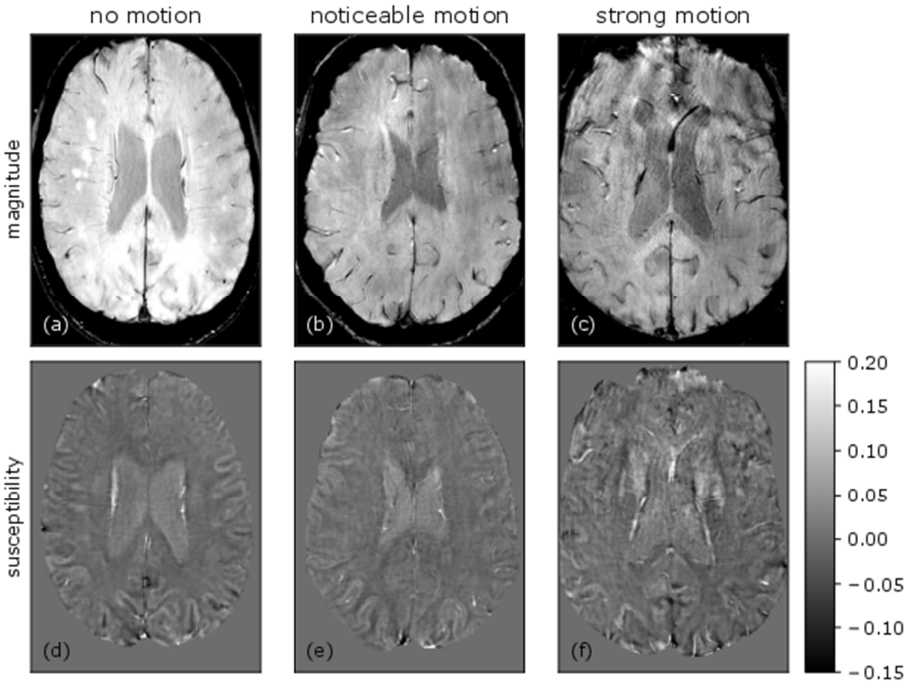

Fig. 2: Example images of the motion categories used for statistics: invisible motion / noticeable motion / strong motion. Images of the upper row (magnitude images at TE=27ms) have been used for categorizing subjects to motion groups. The lower row shows corresponding susceptibility maps, the grayscale mapping to susceptibility values in ppm is shown on the right-hand side.

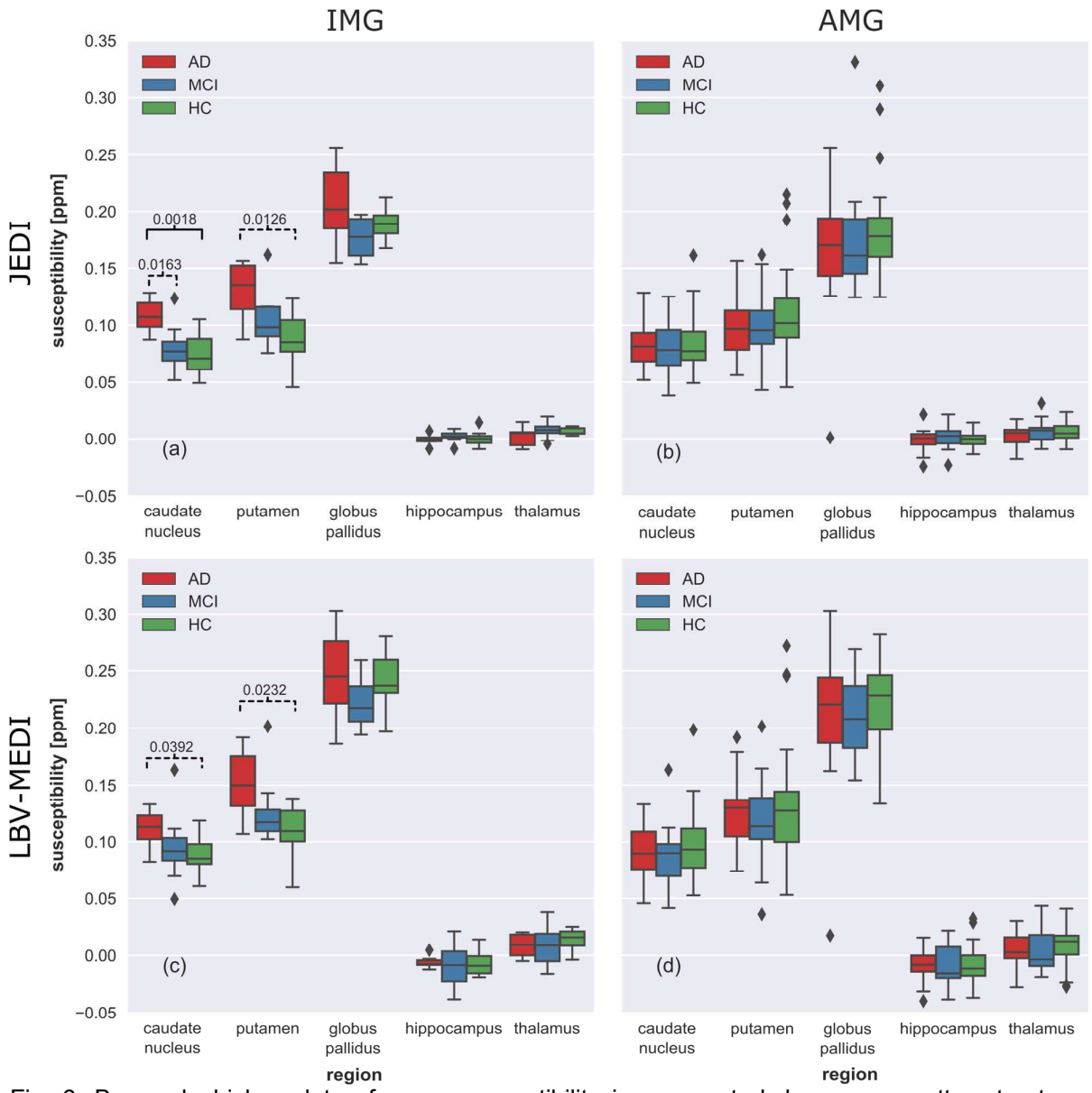

Fig. 3: Box-and-whisker plots of mean susceptibility in segmented deep gray matter structures. Solid (dashed) brackets indicate statistically significant susceptibility differences with (without) Bonferroni correction, p-values without Bonferroni correction are shown next to the brackets. Plots are shown for (a,c) IMG and (b,d) AMG and for two different reconstruction algorithms (a,b) JEDI and (c,d) LBV-MEDI. For both reconstruction algorithms, no statistically significant susceptibility differences are found for AMG. Results for all brain regions investigated are summarized in Tab. 2.